Direct observation of an extended X-ray jet at z=6.1

L. Ighina[1,2], A. Moretti[1], F. Tavecchio[3], A. Caccianiga[1], S. Belladitta[1,2], D. Dallacasa[4,5], R. Della Ceca[1], T. Sbarrato[3], and C. Spingola[5]

[1] INAF – Osservatorio Astronomico di Brera, via Brera 28, 20121, Milano, Italy
e-mail: `lighina@uninsubria.it`
[2] DiSAT – Università degli Studi dell'Insubria, via Valleggio 11, 22100 Como, Italy
[3] INAF – Osservatorio Astronomico di Brera, via E. Bianchi 46, 23807 Merate, Italy
[4] Department of Physics and Astronomy, Università degli Studi di Bologna, Via Gobetti 93/2, 40129 Bologna, Italy
[5] INAF – Institute for Radioastronomy, via Gobetti 101, 40129, Bologna, Italy

ABSTRACT

We report on the direct observation of an extended X-ray jet in the z=6.1 radio-loud Active Galactic Nucleus PSO J030947.49+271757.31 from a deep Chandra X-ray observation (128 ksec). This detection represents the most distant kpc off-nuclear emission resolved in the X-rays to date. The angular distance of the emission is ∼4″(corresponding to ∼20 kpc at z=6.1), along the same direction of the jet observed at parsec scales in previous VLBA high-resolution radio observations. Moreover, the 0.5-7.0 keV isophotes coincide with the extended radio emission as imaged by the VLA Sky Survey at 3 GHz. The rest-frame 2–10 keV luminosity of the extended component is $L_{2-10keV}$=5.9×10^{44} erg s^{-1}, about 8% of the core: this makes it one of the most luminous jets resolved in the X-rays so far. Through Spectral Energy Distribution modelling we find that this emission can be explained by the Inverse Compton interaction with the photons of the Cosmic Microwave Background assuming that the jet's physical parameters are similar to those in the local Universe. At the same time, we find that the radiation produced by a putative population of high-energetic electrons through the synchrotron process observed at low redshift is quenched at high redshift, hence becoming negligible.

Key words. Galaxies: active – Galaxies: nuclei – Galaxies: high-redshift – Galaxies: jets – quasars: general – X-rays: general – individual: PSO J030947.49+271757.31

1. Introduction

Active galactic Nuclei (AGNs) are the brightest permanent astronomical objects and one of the most valuable sources of information from the early Universe. A fraction of them (∼10-15%, e.g. Liu et al. 2021, Diana et al. submitted) is able to expel part of the accreting matter in the form of two collimated relativistic jets originating very close to the supermassive black hole (SMBH) and extending even up to a few Mpc (e.g. Blandford et al. 2019). Understanding the mechanisms responsible for the launch and emission of these jets is of crucial importance to constrain the kinetic power they carry and therefore their feedback on the intergalactic medium as a function of redshift (e.g. Nesvadba et al. 2007; Fabian 2012), as well as to constrain the cosmological evolution of the SMBHs hosted in jetted AGNs (e.g. Fabian et al. 2014) and the relative contribution of jets to the reionisation of the Universe at z>6 (e.g. Torres-Albà et al. 2020).

Even though we are able to resolve the emission and the structure of relativistic jets up to mas scales with radio observations (e.g. Boccardi et al. 2017), in the X-rays we usually observe only the unresolved emission produced in the innermost compact region of the jet, in particular when it is closely aligned to our line of sight (i.e. blazars; e.g. Bhatta et al. 2018). However, there are a few exceptions where, thanks to the angular resolution of the *Chandra* X-ray telescope (∼0.5″; Weisskopf et al. 2000), we are able to resolve the most extended regions of relativistic jets in the X-ray band and therefore to study their properties even at high energies.

Nevertheless, more than 20 years after the direct detection and study of the first extended jet observed with the *Chandra* telescope in the X-rays (Schwartz et al. 2000), there is no homogeneous consensus on the mechanism responsible for the radiation observed several kpc away from the SMBH. One of the first and most popular interpretations proposed for the extended high energy emission is the interaction of the electrons with the photons of the Cosmic Microwave Background (CMB) through Inverse Compton (IC/CMB) (e.g. Tavecchio et al. 2000; Celotti et al. 2001). Despite an initial success of this model, the non-detections of a strong and permanent γ-ray emission from sources in the local Universe (z<1) ruled out the possibility that this process is the main contributor to the observed X-ray emission in most objects (e.g. Meyer et al. 2015; Breiding et al. 2017). At the same time, synchrotron emission from a second highly-energetic population of electrons, different from the one responsible for the radio one, seems to be favoured (Harris & Krawczynski 2002; Jester et al. 2002; Georganopoulos et al. 2006). In any case, we still expect the IC/CMB interaction to take place to a certain degree, especially at high redshift, thanks to the strong evolution of the CMB energy density, ∝(1+z)^4 (e.g. Ighina et al. 2021). For this reason the best way to characterise this interaction and its contribution to the overall X-ray emission is to focus on the high-z jetted AGN population and then to extrapolate the expected amount to lower redshifts (Worrall et al. 2020), where many extended jets have already been analysed (e.g. Harris & Krawczynski 2006; Marshall et al. 2011). At the same time, the IC/CMB radiation is also strongly dependent

on the viewing angle (more than the synchrotron one, e.g. Worrall 2009) and can therefore be more easily observed in blazars, where the relativistic jet is oriented close to the line of sight, even if they are in the local Universe (e.g. Meyer et al. 2019).

In this context, the highest redshift flat-spectrum radio quasar (hereafter simply blazar) known to date, PSO J030947.49+271757.31 (hereafter PSO J0309+27; Belladitta et al. 2020), is the ideal candidate to search for and study the emission of jets on the kiloparsec scale in the primordial Universe and, to this end, we performed relatively deep *Chandra* X-ray observations (128 ksec, P.I. A. Moretti, Archive Seq. Num. 704032, 704242). PSO J0309+27 was discovered by combining the NRAO VLA Sky Survey (NVSS at 1.4 GHz; Condon et al. 1998) with the Panoramic Survey Telescope and Rapid Response System (PanSTARRS; Chambers et al. 2016) and then confirmed spectroscopically (Belladitta et al. 2020). Based on the flat radio spectrum in the 0.15–1.4 GHz observed band and the high X-ray luminosity derived from a *Swift*-XRT observation, this source was classified as a blazar, the first observed at *z*>6. Thanks to its very bright nature compared to other *z*>6 AGNs, PSO J0309+27 has been the target of several observational campaigns aimed at constraining the full extent of its Spectral Energy Distribution (SED), see Belladitta et al. (2020); Spingola et al. (2020); Moretti et al. (2021); Belladitta et al. submitted and also Mufakharov et al. (2021). In this work we focus on the multiwavelength characterisation of the emission extending a few arcsec from the AGN position, which was revealed from dedicated X-ray *Chandra* observations and which represents the highest redshift jet resolved in the X-rays currently known.

In section 2 we present the radio and optical data available that can constrain the arcsec emission of PSO J0309+27 as well as the X-ray imaging and spectral analysis of the *Chandra* observations. In section 3 we model the X-ray and radio measurements considering both the IC/CMB interaction as well as the synchrotron emission of an highly energetic population of electrons. We then compare currently available data for the extended jet of PSO J0309+27 to other resolved jets at lower redshift reported in the literature. Finally, in section 4 we summarise our results and conclusions.

Throughout the paper we assume a flat ΛCDM cosmology with H_0=70 km s^{-1} Mpc^{-1}, Ω_m=0.3 and Ω_Λ=0.7, where 1″ corresponds to a projected distance of 5.66 kpc at *z*=6.1. Spectral indices are given assuming $S_\nu \propto \nu^{-\alpha}$ and all uncertainties are reported at 90% confidence, unless otherwise specified.

2. Multiwavelength Data

In this section we describe the archival and recent proprietary data for PSO J0309+27 relevant to the study of the source's jet at arcsec resolution. A detailed discussion on the components at scales ≲1″ is given by Spingola et al. (2020) in the radio, Belladitta et al. submitted in the optical/near-infrared (NIR) and Moretti et al. (2021) in the X-rays.

2.1. Radio observations

Besides the NVSS survey, PSO J0309+27 was detected in the TIFR Giant Metrewave Radio Telescope Sky Survey (TGSS; Intema et al. 2017) at 150 MHz and in The Karl G. Jansky Very Large Array Sky Survey (VLASS; Lacy et al. 2020) at 3 GHz. In both these surveys an extended component is visible in the
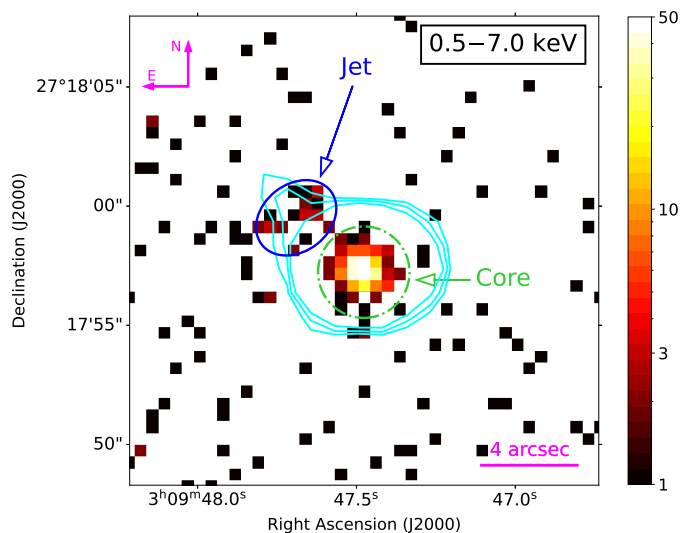
Fig. 1. 3 GHz radio contours from the VLASS survey (in cyan) overlaid on the 0.5–7 keV X-ray image of PSO J0309+27 from the 128 ksec *Chandra* observation. The counts colour scale is displayed on the right. For displaying purposes, only the (3, 3 $\sqrt{2}$, 6) × the off-source RMS (=0.12 mJy beam^{-1}) radio contours are reported. The dashed green circle and the solid blue ellipse are the regions used for the extraction of the core and the jet X-ray spectra respectively.

North-East direction (NE). In the TGSS image, the extended structure is possibly observed up to ∼20″ (∼110 kpc), although the signal-to-noise ratio is low (∼2; see Fig. 3 in Belladitta et al. 2020); in the VLASS image the extension is present ∼4″ from the core with a ∼5×RMS significance: S_{peak}=0.63 mJy beam^{-1} (RMS=0.12 mJy beam^{-1}; see Fig. 1). In this work we considered this latter value for the radio emission of the kpc jet by adding a further 10% to the uncertainty since the VLASS quick-look images flux calibration may be less reliable for faint sources (see Gordon et al. 2020 for more details).

Moreover, PSO J0309+27 was the target of Very Long Baseline Array (VLBA) observations at 1.5, 5 and 8.4 GHz in April 2020. From these radio observations at milliarcsecond angular resolution, Spingola et al. (2020) discovered the presence of a jet which extends for about 500 pc in projection in the NE direction as well (magenta dashed line in Fig. 2). At the same time, low-resolution observations (between 22″, at 1.4 GHz, and 1″, at 40 GHz) of PSO J0309+27 with the Jansky VLA revealed that the overall radio spectrum of the source is relatively steep (α_r ∼1; Spingola et al. 2020), indicating that its total radio emission is not dominated by the innermost regions of the jet.

2.2. Optical/near-infrared observations

In the optical and NIR bands the field around PSO J0309+27 was observed in the PanSTARRS survey (in the *g*, *r*, *i*, *z* and *Y* filters) as well as through dedicated observations with the Telescopio Nazionale Galileo (TNG) in the *J* and K_p filters (P.I. S. Belladitta; see Fig. 2 and Belladitta et al. submitted for further details). The corresponding 3σ limiting magnitudes for an extended object of the size of the resolved X-ray photons (see Fig. 1 and next sub-section) range from 23.2 to 21.2 mag. In all these observations, as well as in the Wide-field Infrared Survey Explorer catalogue (catWISE; Eisenhardt et al. 2020), no optical/IR counterpart associated with the extended jet is observed, suggesting that the observed X-ray emission is likely related to the
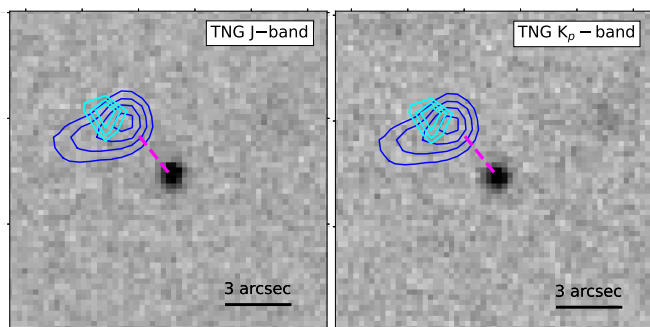
Fig. 2. *J* and *K*$_p$–band images of PSO J0309+27 obtained with the TNG. The contours of the smoothed Chandra X-ray image, with the core's region subtracted, are shown in blue; while the contours from the residual (i.e. with the core's emission subtracted) VLASS image are displayed in cyan. The contours level have been arbitrarily chosen to best show the jet and are always greater than 3×RMS of the given image. The magenta dashed line indicates the direction of the ∼500 pc radio jet described in Spingola et al. (2020).

jet of PSO J0309+27 and not to a foreground/background source such as an obscured active galaxy.

2.3. Chandra X-ray imaging and spectral analysis

2.3.1. Astrometry

PSO J0309+27 has been observed for a total of 128 ksec with the *Chandra* telescope, (26.7 ksec in March 2020 and 101.7 ksec in November 2020). Data reduction was performed using the *Chandra* Interactive Analysis of Observations software package (CIAO, v4.13; Fruscione et al. 2006) with CALDB version 4.9.5. The final image was reconstructed correcting the astrometry of the single observation segments. To this end we used the position of five objects detected both in PanSTARRS and in the Chandra observation. The transformation matrix was produced through the wcs_match task. We found typical shifts of +0.7 and +0.9 pixels (1 pixel=0.492″) in RA and DEC respectively, with no significant rotation. This is not unexpected, given that the overall 68% uncertainty circle of Chandra X-ray absolute position has a radius of 0.6″[1]. Astrometry of the event file and images has been modified accordingly by means of the wcs_match task. PSO J0309+27 is detected with 320 photons in the 0.5-7.0 keV band within a 2″radius circle (98% of the PSF) with only ∼2.7 background photons expected. With the corrected astrometry the position of the X-ray source is RA=47.44786 deg and DEC=+27.29922 deg with an error of 0.2″, mostly due to the residuals in the astrometric correction. This position is consistent with the PanSTARRS optical and the VLASS/VLBA radio positions.

2.4. X-ray Imaging

In Fig. 1 we report the X-ray image obtained from the overall 128 ksec exposure in the 0.5–7 keV energy band with the radio contours at 3 GHz (from the VLASS survey) overlaid. In Fig. 2 we show the residual of the X-ray and radio images after the subtraction of the core emission (assumed to be point-like) overlaid on the NIR images. After the removal of the X-ray core, a significant excess of photons is present between 2-5″away from the position of PSO J0309+27. Moreover, there is an overall positional

agreement between the extended components in the X-rays and in the radio, both directed towards the NE direction, similar to the position angle of the jet described in Spingola et al. (2020) at parsec scales.

We note that, even though radio data are too shallow for any detailed study, the jet seems to be resolved in the X-rays with a lower surface brightness component towards the eastern direction. Such tangential extension could be related to a potential bend at kpc scales. Indeed, if the jet was oriented close to our line of sight (as hinted by the multiwavelength properties of PSO J0309+27, e.g. Spingola et al. 2020; Moretti et al. 2021), even a small re-orientation of the jet would be amplified through projection and would result in a significant apparent change of direction. Similar bends have already been observed in the jets of several quasars, both at pc (in the radio band, e.g. Lister et al. 2021) and at kpc scales (in the radio and X-ray bands, e.g. Worrall & Birkinshaw 2005; Marshall et al. 2011). Therefore it is likely that the overall extended X-ray emission of PSO J0309+27 visible in Fig. 2 is associated with different regions of the relativistic jet, before and after the bend. Nevertheless, deeper X-ray and radio observations at arcsec resolution are needed to confirm this hypothesis and to fully characterise the morphology of this kpc jet. For simplicity in the following we consider the entire extended emission to be produced in regions with similar physical properties.

In order to qualitatively constrain the projected size of the emitting region, we started by computing the number of photons observed per unit of area around the core of PSO J0309+27 as a function the distance. We show in Fig. 3 the radial profile obtained. We also report the expected distribution for a point-like source with an X-ray spectrum given by the core of PSO J0309+27 (see next sub-section). In order to simulate the PSF of the core alone we used the Model of AXAF Response to X-rays (MARX, version 5.5) Chandra end-to-end science simulator through the CIAO task simulate_psf. In particular, we averaged the simulated PSF over 1000 trials with the core's spectrum normalised at ×100 its actual flux as input, in order to increase the statistics. From the comparison of the expected PSF and the observed radial distribution, it is clear that up ∼2.5″ PSO J0309+27 is consistent with being a point-like source, whereas at larger radii there is a statistically significant abundance of observed X-ray photons (see Fig. 3 top). In particular, the observed number of photons enclosed in each annulus is 5-10 times larger than what expected from a point-source alone.

At the same time, by computing the angular profile of the photons detected in 20 sectors with an inner and outer radius of 2–10″, we find that the observed extended X-ray emission has an angular aperture of ∼50 deg centred at a position angle (P.A.) of 55 deg. Interestingly, the number of photons observed in the opposite direction, where the counter-jet is expected, is consistent with the background level, thus confirming that we are observing the source at an angle close to the jet's axis. Based on the distributions reported in Fig. 3, throughout the paper we consider the jet to have a radial and angular extension of 2.5″(from *r*=2.5″to *r*=5″) and 4″ (from P.A.=25 deg to P.A.=80 deg) respectively. Assuming a viewing angle of $\theta_v \sim 20°$ (see next section) this projected distance, 15-30 kpc at *z*=6.1, corresponds to a de-projected size of 40-90 kpc.

2.5. X-ray Spectral Analysis

Based on the values reported in the previous section, the region we adopted for the X-ray spectral analysis is reported with a
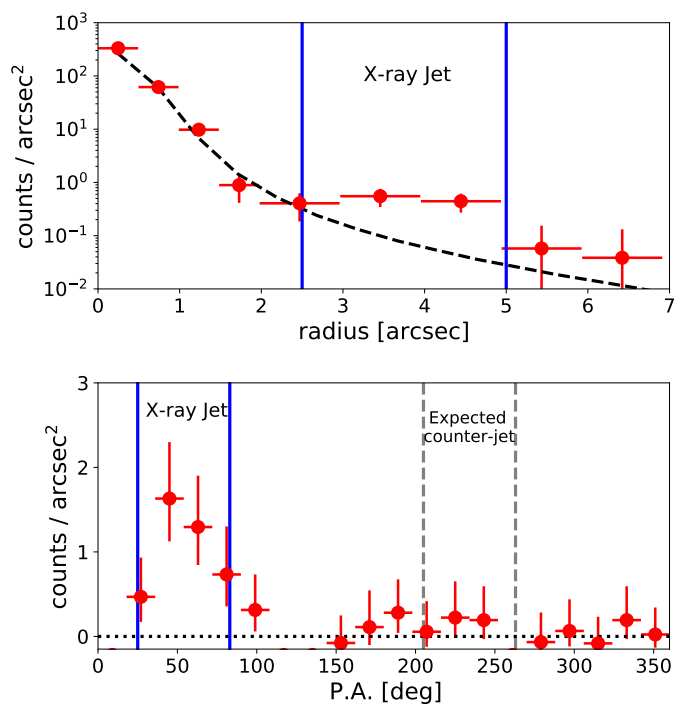
---

[1] https://cxc.cfa.harvard.edu/cal/ASPECT/celmon/

Fig. 3. The observed radial (top) and angular (bottom) profiles of PSO J0309+27 in the 0.5–7 keV energy band. In both cases the background has been subtracted and data points have Poissonian uncertainties. The dashed black line in the top panel is the expected PSF of the observation, computed with MARX. The vertical blue lines delimit the extraction region considered for the spectral analysis of the jet, while the area delimited by the grey lines is where the counter-jet is expected (see sec. 2.3.2). The direction of the P.A. in the lower panel is East of North.

solid blue ellipse in Fig. 1 and contains a total of 27 photons between 0.5 and 7 keV.

The analysis of the extended jet was performed in a similar way to the one of the core described in Moretti et al. (2021). Using the SPECEXTRACT task we extracted the core and jet counts from the two regions reported in Fig. 1, while for the background we considered an annulus between 12″and 25″centred at the position of the AGN. We then analysed the extracted spectra using the XSPEC (v12.11.1) package and performed a fit to both the core and the jet emission in the energy range 0.5-7 keV (in order to reduce the background noise) with a power law absorbed by the Galactic column density along the line of sight (N$_H$=1.13×10^{21} cm^{-2}; HI4PI Collaboration et al. 2016) and adopting the C-statistics (Cash 1979). We report in Tab. 1 the results of the analysis. In the case of the core analysis, the "flaring" intervals described in Moretti et al. (2021) have not been considered. In Fig. 4 we report the X-ray spectra of the core and the extended jet of PSO J0309+27 modelled as described above. As already noted by Belladitta et al. (2020) the X-ray properties of the core (Γ$_{core}$=1.65 and α$_{ox}$=1.13, α̃$_{ox}$=1.02[2]) suggest that the observed X-ray emission is dominated by the beamed radiation produced within the jet oriented close to the line of sight (i.e. it is likely a blazar; e.g. Ghisellini 2015; Ighina et al. 2019). The overall X-ray-to-radio ratio (L$_{2-10keV}$/L$_{1.4GHz}$=2.76) is also consistent with the trend of increasing X-ray luminosities as a function of redshift observed up to z~5.5 in Ighina et al. (2021), which may be attributed to an increase of the total X-ray emis-

[2] defined as: α$_{ox}$=-0.384 log $\frac{L_{2keV}}{L_{2500Å}}$ and α̃$_{ox}$=-0.303 log $\frac{L_{10keV}}{L_{2500Å}}$.
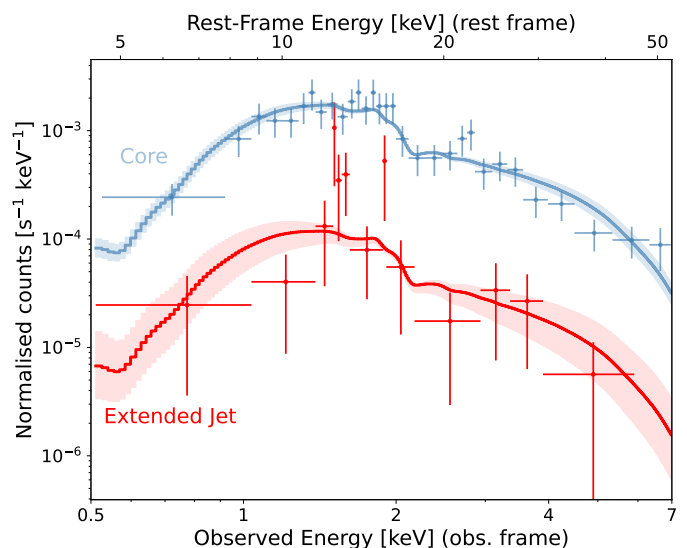

Fig. 4. Folded X-ray spectrum of the core (top, in blue) and of the extended jet (bottom, in red) of PSO J0309+27. Data are binned at a 2σ significance for displaying purposes only. In both cases data were fitted with a Galactic absorbed power law. The best-fit spectra are reported as solid lines, while the shaded areas represent their 90% confidence uncertainties.

sion (resolved and not) due to the IC/CMB interaction.

The off-nuclear X-ray emission presents a relatively flat slope (Γ$_{jet}$=1.79), which suggests that the population of electrons did not suffer significant energy losses yet (e.g. Achterberg et al. 2001). Its rest-frame luminosity, L$_{2-10keV}$=5.91×10^{44} erg sec^{-1}, corresponds to ~8% of the core's one, making it one of the least core-dominated AGNs in the X-rays (e.g. Snios et al. 2021) and at the same time one of the most X-ray luminous extended jet observed to date (e.g. McKeough et al. 2016).

Table 1. Best-fit parameters derived from the X-ray analysis of both the jet and core component shown in Fig. 1. In both cases a simple power law with only Galactic absorption is assumed (N$_H$=1.13×10^{21} cm^{-2}; HI4PI Collaboration et al. 2016).

	Γ	f$_{0.5-7keV}$ 10^{-15} erg s^{-1} cm^{-2}	L$_{2-10keV}$ 10^{44} erg s^{-1}	cstat / d.o.f.
Core:	$1.65^{+0.18}_{-0.18}$	$47.82^{+1.21}_{-0.82}$	$78.33^{+17.02}_{-14.01}$	128.9 / 176
Jet:	$1.79^{+0.74}_{-0.69}$	$3.08^{+0.49}_{-0.30}$	$5.91^{+6.81}_{-3.20}$	26.9 / 20

3. Discussions

The mechanism responsible for the high energy emission observed in large-scale extragalactic jets is still debated. The same electrons emitting in the radio band via synchrotron can be responsible for the observed X-ray flux via IC with the CMB photons (e.g Schwartz et al. 2019). However, this would require that most jets remain relativistic on scales up to 10-100 kpc (e.g. Tavecchio et al. 2000). As a consequence, one would also expect this same interaction to produce bright γ-ray emission. Nevertheless, the non-detection of such radiation with the *Fermi* Large Area Telescope (*Fermi*/LAT) ruled out the IC/CMB as the main responsible for the X-ray radiation produced in the majority of extended jets in the local Universe (e.g. Meyer & Georganopou-

los 2014; Meyer et al. 2015). Therefore, another process must take place to account for the observed X-ray emission of these jets. The most plausible solution is the presence of a second population of electrons, besides the one responsible for the synchrotron radio and IC/CMB X-ray emissions. This population should be accelerated to very high energies ($\gamma \sim 10^8 - 10^9$ or ~100 TeV for magnetic fields of the order of a few μG) and then emit in the X-rays through the synchrotron process (e.g. Atoyan & Dermer 2004; Kataoka & Stawarz 2005). How these electrons can be accelerated up to very high energies far from the jet launch site is not fully understood yet. In the following we consider the scenario detailed in Tavecchio (2021).

3.1. Two electron population model

The model adopted here for the emission of very high energy electrons (presented in Tavecchio 2021) is based on the *shear acceleration* mechanism (e.g. Rieger 2019), in which electrons can be accelerated to ultra-relativistic energies by magnetic turbulence in a shear layer surrounding the main body of the jet (spine). This shear layer is expected to be characterised by a strong radial gradient of the velocity. In these conditions, particles diffusing in the layer experience a continuous energy gain through the scattering by the turbulence moving with different speeds. An important feature of this model is that the acceleration can proceed at a sufficiently fast rate only in the case of highly energetic electrons. Therefore, this mechanism requires a process able to pre-accelerate the electrons. Possible candidates for the pre-acceleration include turbulence in the flow (Liu et al. 2017) or magnetic reconnection triggered by instabilities at the jet boundary (Sironi et al. 2021). Tavecchio (2021) assumes that electrons experiencing shear acceleration are those accelerated by a shocks along the jet (i.e. the ones responsible for the synchrotron emission at low frequency).

Even with a pre-acceleration mechanism, the shear acceleration timescale is relatively long. This feature gives us a simple explanation for the phenomenology observed at both low and high redshift. In fact, at low redshift the relatively small radiative losses allow the electrons in the shear layer to be accelerated up to high energies and therefore to emit in the X-rays through a synchrotron process. At high redshift, where the CMB energy density is much higher, the situation changes, since the cooling time of IC/CMB is significantly shorter than the shear acceleration timescale, even for the most energetic electrons. This severely hampers the acceleration and effectively limits the contribution of the second population to the X-ray emission. At the same time, the increased CMB energy density determines a luminous IC/CMB emission from the low-energy electrons accelerated at the shock which naturally accounts for the bright X-ray emission. In this scheme it is therefore natural to expect that the second electron population can contribute to or even dominate the X-ray emission of low-z jets, while at high redshift the main contribution derives from the IC/CMB emission of the low-energy electron component.

3.2. Application to PSO J0309+27

PSO J0309+27, with its powerful jet at an unprecedented high redshift, represents the ideal laboratory to test the scenario presented above. In order to check the consistency with the theoretical expectations, we compared our data to the two population of electrons model used by Tavecchio (2021) to reproduce the emission of the prototypical extended jet associated with the blazar

PKS J0637−752 at z=0.65. In principle, this model is characterised by many free parameters. However, constraints from jet energetics and acceleration efficiency restrict the range of several parameters. In particular, the magnetic field intensity is constrained by the total energetic and cooling of the electrons around 10 μG. Since the treatment of the acceleration is performed in the non-relativistic limit we assume a relatively small bulk Lorentz factor, $\Gamma_b = 1.7$.

Remarkably, adopting the same parameter values for the jet characteristics (listed in Table 2) that reproduce the emission of PKS J0637−752 at z=0.65 (solid grey line in Fig. 5) and only varying the level of the energy density of the CMB (a factor ~350 increase from z=0.65 to z=6.1), the same model can nicely fit also the PSO J0309+27 data (solid red line in Fig. 5). In the case of PKS J0637−752 the radio and X-ray humps are produced by the synchrotron emissions of the low- and high-energy electron population respectively. The contribution from the IC/CMB emission of the low-energy electrons is almost negligible (dotted grey lines) up to the hard X-ray band. In the γ-ray band the model predicts a component due to the combination of Synchrotron Self-Compton (SSC) and IC/CMB emission of the high-energy component. However, the absorption of the gamma rays by the extragalactic background light (EBL) at optical-UV frequencies determines a narrow cut-off around 50 GeV (~10^{25} Hz). At high redshift (i.e. PSO J0309+27; red lines), the increasing level of the CMB energy density determines the rapid cooling of electrons with Lorentz factor exceeding $\gamma \sim 10^5$. In these conditions the shear acceleration process is basically inactive, while the IC/CMB emission from the low-energy electron component nicely matches the observed X-ray emission.

We note that the relatively small bulk Lorentz factor adopted here is not in contrast with the larger values derived by Spingola et al. (2020) and Moretti et al. (2021) when studying the innermost regions of the jet of PSO J0309+27 in the radio and X-ray band respectively. This is not unexpected since, at very large distances from the central engine (>kpc) the jet likely decelerates (e.g. Bridle et al. 1994; Asada & Nakamura 2012), otherwise large bulk Lorentz factors ($\Gamma_b \gtrsim 5 - 10$) would imply a strong IC/CMB γ-ray emission detectable by the *Fermi*/LAT, which has not been observed in the majority of the extended jets in the local Universe (e.g. Meyer et al. 2015).

3.3. Redshift evolution of the extended X-ray emission

The two cases analysed in the previous sub-section represent two extremes of a continuous sequence regulated by the CMB energy density (i.e. redshift). In order to show the dependency of the kpc jet emission as a function of redshift and to facilitate the comparison with other studies on extended jets, we the adopt the X-ray-to-radio flux ratio ($\nu_X S_X/\nu_r S_r$) as well as the corresponding α_{rx} parameter, defined as the slope of a power law connecting the radio and X-ray emission in the observed frame (e.g. Marshall et al. 2005):

$$\alpha_{rx} = -\frac{\log(S_X/S_r)}{\log(\nu_X/\nu_r)} = 1 - \frac{\log(\nu_X S_X/\nu_r S_r)}{\log(\nu_X/\nu_r)} \qquad (1)$$

In both cases the values are taken at 1 keV and at 3 GHz in the observed frame. The X-ray and radio flux densities of PSO J0309+27 were extracted from the *Chandra* and VLASS images and are reported in Table 3 together with the X-ray-to-radio flux and the jet-to-core (both X-ray and radio) ratios.

In Fig. 6 we show the evolution of the X-ray-to-radio ratio based on the model described above as a function of redshift

Γ_b	θ	γ_{cut} ($\times 10^5$)	K	n_{sh}	B	δ	R	τ_{inj}	t	P_{jet}
[1]	[2]	[3]	[4]	[5]	[6]	[7]	[8]	[9]	[10]	[11]
1.7	20	4	0.45	2.5	13	2.5	2×10^{21}	5×10^2	10	2.2

Table 2. Parameters of the model. [1]: jet bulk Lorentz factor; [2]: viewing angle (deg); [3]: cut-off electron Lorentz factor of the shock component; [4]: normalization of the the shock electron energy distribution (particle cm^{-3}); [5]: slope of the the shock electron energy distribution; [6]: magnetic field (μG); [7]: Doppler factor; [8]: jet radius (cm); [9]: injection timescales for the shear acceleration in units of the light-crossing time r_j/c (where r_j is the radius of the jet); [10]: time in units of the light-crossing time r_j/c. [11]: jet power (10^{46} erg s^{-1}).

Table 3. X-ray and radio properties of the extended jet of PSO J0309+27 extracted from the *Chandra* and VLASS images. The errors are reported at 90% confidence.

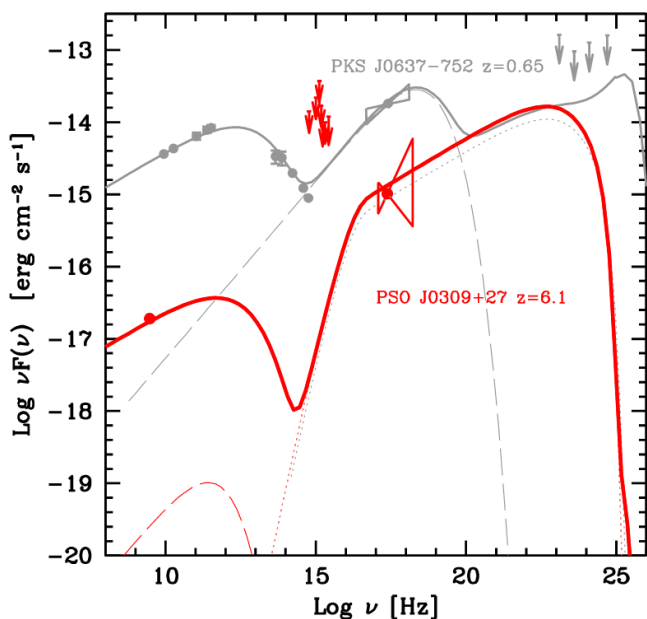| S_{1keV} (nJy)	S_{3GHz} (mJy)	α_{rx}	$\nu_X S_X/\nu_r S_r$	$(L_{jet}/L_{core})_X$	$(L_{jet}/L_{core})_r$
$0.42^{+0.21}_{-0.18}$	0.63 ± 0.20	-0.78 ± 0.03	54^{+32}_{-29}	8%	5%

Fig. 5. Observed SED of the extended emission of the source PKS J0637−752 at z=0.65 (grey points), based on which the physical parameters of the model have been set (grey lines). The red lines show the same model but at the redshift of PSO J0309+27, z=6.1. The X-ray, optical/NIR and radio measurements or upper limits of the extended jet emission in PSO J0309+27 are shown as red points and arrows and the ones of PKS J0637−752 are shown as grey points and arrows. In grey we also show the upper limits from *Fermi*/LAT, for both sources. We stress that the only difference between the input parameters of the two curves is the redshift. At low-z the extended X-ray emission is dominated by the synchrotron component (dashed lines) of the second population of electrons accelerated up to ultra-high energies ($\gamma \sim 10^{8-9}$). Whereas at high-z, electrons are cooled down by the IC/CMB interaction much faster than they can be accelerated and thus the IC/CMB emission (dotted lines) dominates in the X-rays while the synchrotron emission is significantly quenched.

(solid red line). As explained in the previous sub-section, while at low redshift (PKS J0637−752, orange cross) the high-energy synchrotron emission dominates the observed X-ray range, at high redshift (PSO J0309+27, red star) the only mechanism able to efficiently produce the observed extended X-ray emission is the IC/CMB. Based on the parameters adopted here, the transition between the two mechanisms is expected to be around $z\sim2$. Beyond this value the peak of the high-energy synchrotron emis-

sion shifts below the X-ray band due to cooling and therefore its contribution to the total radiation observed is negligible (dashed black line). At the same time, the increase of the CMB energy density boosts the IC/CMB emission, which becomes dominant at $z>2$ (dotted blue line), where we expect to observe its typical evolutionary trend $\propto(1+z)^{3+\alpha}$ (e.g. Worrall 2009). This is consistent with the other detailed studies on extended jets at $z\sim3$-4 (e.g. Cheung et al. 2012; Worrall et al. 2020).

In Fig. 6 we also compare the relative X-ray intensity of the extended emission with respect to the radio one for PSO J0309+27 to the other resolved jets in AGNs at lower redshift available in the literature. All the comparison sources are quasars, similarly to PSO J0309+27. If radio data were taken at a different frequency with respect to PSO J0309+27, we computed the corresponding flux density at 3 GHz assuming a radio spectral index of α_r=1, as typically observed in spatially resolved jets at kpc scales (e.g. Cheung et al. 2006, 2012). Data are largely scattered, probably reflecting the wide variety of the physical properties of the jets and their components. As noted by previous authors (e.g. McKeough et al. 2016; Marshall et al. 2018), although low values of the X-ray-to-radio ratio are not observed at high redshift, the correlation with redshift is not highly significant. In particular, the sources at $z>2$ do not belong to a single complete sample and the values reported in the literature are often biased towards objects with a strong X-ray jet since many of them are detections resulted from very short *Chandra* observations ($\sim$10 ksec; e.g. Snios et al. 2021). As a reference, we also show the limit above which extended jets with similar radio properties (i.e. radio luminosity) to PSO J0309+27 can be detected with a relatively deep (100 ksec) *Chandra* observation (solid green line).

4. Summary and Conclusions

In this work we presented the X-ray detection and analysis of the most distant kpc jet spatially resolved, at z=6.1. From dedicated *Chandra* observations we found that the X-ray emission extends up to about 4″, equal to a de-projected linear size of $\sim$70 kpc (assuming $\theta_v \sim 20^o$). This kpc jet is characterised by a high luminosity ($L_{2-10keV}$=5.9$^{+6.8}_{-3.2}$$\times10^{44}$ erg s^{-1}) as well as one of the largest core-to-jet ratio (8%). Moreover, from the detection of this extended component in the VLASS radio survey, we were also able to constrain its SED and its X-ray-to-radio ratio. The very-high redshift of PSO J0309+27 makes it an ideal source to test the redshift evolution of the emission in extended jets expected from the IC/CMB trend.
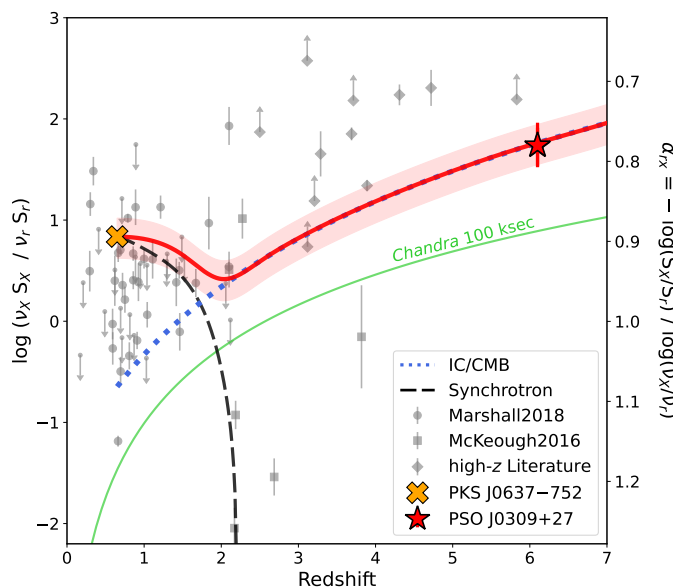
Fig. 6. X-ray-to-radio ratios (and α_{rx}) of the extended jets observed by *Chandra* reported in the literature. The data are from: Marshall et al. (2018), circles at $z \lesssim 2$; McKeough et al. (2016), squares at $2 \lesssim z \lesssim 4.7$ (given by the sum of their "detected" components); Siemiginowska et al. (2003); Cheung et al. (2006); Simionescu et al. (2016); Schwartz et al. (2020); Worrall et al. (2020); Snios et al. (2021); Connor et al. (2021), diamonds at $z \gtrsim 3$. If the same object is reported in more than one work we consider the most recent one. PSO J0309+27 ($z=6.1$) is represented by a red star, while PKS J0637−752 ($z=0.65$) by an orange cross. The solid red line connecting the two sources is the evolution of the X-ray-to-radio ratio as a function of redshift based on the model reported in Fig. 5, where the extended X-ray emission is given by the sum of a synchrotron (dashed black line) and an IC/CMB component (dotted blue line). The green solid line represents the limit above which an extended X-ray jet with the same radio luminosity of the one found in PSO J0309+27 can be observed with a 100 ksec *Chandra* exposure.

By comparing the X-ray-to-radio flux ratio of PSO J0309+27 to the other extended jets analysed in the literature we found that the value derived for PSO J0309+27 is larger than what is typically measured in the local Universe (e.g. Marshall et al. 2018), as expected from the IC/CMB model. Indeed, assuming physical parameters with values typically seen in the local Universe and only mild relativistic boosting ($\Gamma_b \sim 1.7$), the multiwavelength emission of the jet of PSO J0309+27 is fully consistent with the IC/CMB interaction of the same electrons responsible for the synchrotron radiation in the radio band.

Although similar conclusions were drawn for a few sources at $z \sim 3-4$ (e.g. Worrall et al. 2020), we also argue that IC/CMB is the only mechanism able to efficiently produce the X-ray extended emission observed at these redshifts. Indeed, we found that the expected contribution to the extended X-ray emission from a second population of electrons (modelled as discussed in Tavecchio 2021) is naturally quenched at high redshift since the time needed by the electrons to be accelerated up to very high energies becomes larger than the IC/CMB cooling time. In particular, we showed how the high-energy synchrotron model can reproduce the radio-to-X-ray emission in jets up to $z \sim 2$, after which the redshift dependence of the CMB energy density has a double effect on the two populations of electrons: on the one side it enhances the X-ray (and γ-ray) radiation produced through IC/CMB by the low-energy population; on the other side it cools more efficiently the most energetic electrons which, in turn, cannot be accelerated up to energies needed to produced

synchrotron X-ray emission. Despite the general good consistency of this picture with the observations collected so far, detailed studies of statistical samples of high-z jets (with both radio and X-ray data) need to be performed in order to put this result on a more solid basis.

References

Achterberg, A., Gallant, Y. A., Kirk, J. G., & Guthmann, A. W. 2001, MNRAS, 328, 393
Asada, K. & Nakamura, M. 2012, ApJ, 745, L28
Astropy Collaboration, Price-Whelan, A. M., Sipőcz, B. M., et al. 2018, AJ, 156, 123
Atoyan, A. & Dermer, C. D. 2004, ApJ, 613, 151
Belladitta, S., Moretti, A., Caccianiga, A., et al. 2020, A&A, 635, L7
Bhatta, G., Mohorian, M., & Bilinsky, I. 2018, A&A, 619, A93
Blandford, R., Meier, D., & Readhead, A. 2019, ARA&A, 57, 467
Boccardi, B., Krichbaum, T. P., Ros, E., & Zensus, J. A. 2017, A&A Rev., 25, 4
Breiding, P., Meyer, E. T., Georganopoulos, M., et al. 2017, ApJ, 849, 95
Bridle, A. H., Hough, D. H., Lonsdale, C. J., Burns, J. O., & Laing, R. A. 1994, AJ, 108, 766
Cash, W. 1979, ApJ, 228, 939
Celotti, A., Ghisellini, G., & Chiaberge, M. 2001, MNRAS, 321, L1
Chambers, K. C., Magnier, E. A., Metcalfe, N., et al. 2016, eprint arXiv:1612.05560 [arXiv:1612.05560]
Cheung, C. C., Stawarz, Ł., & Siemiginowska, A. 2006, ApJ, 650, 679
Cheung, C. C., Stawarz, Ł., Siemiginowska, A., et al. 2012, ApJ, 756, L20
Condon, J. J., Cotton, W. D., Greisen, E. W., et al. 1998, AJ, 115, 1693
Connor, T., Bañados, E., Stern, D., et al. 2021, arXiv e-prints, arXiv:2103.03879
Eisenhardt, P. R. M., Marocco, F., Fowler, J. W., et al. 2020, ApJS, 247, 69
Fabian, A. C. 2012, ARA&A, 50, 455
Fabian, A. C., Walker, S. A., Celotti, A., et al. 2014, MNRAS, 442, L81
Fruscione, A., McDowell, J. C., Allen, G. E., et al. 2006, in Society of Photo-Optical Instrumentation Engineers (SPIE) Conference Series, Vol. 6270, Society of Photo-Optical Instrumentation Engineers (SPIE) Conference Series, ed. D. R. Silva & R. E. Doxsey, 62701V
Georganopoulos, M., Perlman, E. S., Kazanas, D., & McEnery, J. 2006, ApJ, 653, L5
Ghisellini, G. 2015, Journal of High Energy Astrophysics, 7, 163
Gordon, Y. A., Boyce, M. M., O'Dea, C. P., et al. 2020, Research Notes of the American Astronomical Society, 4, 175
Harris, D. E. & Krawczynski, H. 2002, ApJ, 565, 244
Harris, D. E. & Krawczynski, H. 2006, ARA&A, 44, 463
HI4PI Collaboration, Ben Bekhti, N., Flöer, L., et al. 2016, A&A, 594, A116
Ighina, L., Caccianiga, A., Moretti, A., et al. 2019, MNRAS, 489, 2732
Ighina, L., Caccianiga, A., Moretti, A., et al. 2021, MNRAS, 505, 4120
Intema, H. T., Jagannathan, P., Mooley, K. P., & Frail, D. A. 2017, A&A, 598, A78
Jester, S., Röser, H. J., Meisenheimer, K., & Perley, R. 2002, A&A, 385, L27
Kataoka, J. & Stawarz, Ł. 2005, ApJ, 622, 797
Lacy, M., Baum, S. A., Chandler, C. J., et al. 2020, PASP, 132, 035001
Lister, M. L., Homan, D. C., Kellermann, K. I., et al. 2021, ApJ, 923, 30
Liu, R.-Y., Rieger, F. M., & Aharonian, F. A. 2017, ApJ, 842, 39
Liu, Y., Wang, R., Momjian, E., et al. 2021, ApJ, 908, 124
Marshall, H. L., Gelbord, J. M., Schwartz, D. A., et al. 2011, ApJS, 193, 15
Marshall, H. L., Gelbord, J. M., Worrall, D. M., et al. 2018, ApJ, 856, 66
Marshall, H. L., Schwartz, D. A., Lovell, J. E. J., et al. 2005, ApJS, 156, 13
McKeough, K., Siemiginowska, A., Cheung, C. C., et al. 2016, ApJ, 833, 123
Meyer, E. T. & Georganopoulos, M. 2014, ApJ, 780, L27
Meyer, E. T., Georganopoulos, M., Sparks, W. B., et al. 2015, ApJ, 805, 154
Meyer, E. T., Iyer, A. R., Reddy, K., et al. 2019, ApJ, 883, L2
Moretti, A., Ghisellini, G., Caccianiga, A., et al. 2021, ApJ, 920, 15
Mufakharov, T., Mikhailov, A., Sotnikova, Y., et al. 2021, MNRAS, 503, 4662

Nesvadba, N. P. H., Lehnert, M. D., De Breuck, C., Gilbert, A., & van Breugel, W. 2007, A&A, 475, 145

Rieger, F. M. 2019, Galaxies, 7, 78

Schwartz, D., Siemiginowska, A., Worrall, D., et al. 2019, Astronomische Nachrichten, 340, 30

Schwartz, D. A., Marshall, H. L., Lovell, J. E. J., et al. 2000, ApJ, 540, 69

Schwartz, D. A., Siemiginowska, A., Snios, B., et al. 2020, ApJ, 904, 57

Siemiginowska, A., Smith, R. K., Aldcroft, T. L., et al. 2003, ApJ, 598, L15

Simionescu, A., Stawarz, Ł., Ichinohe, Y., et al. 2016, ApJ, 816, L15

Sironi, L., Rowan, M. E., & Narayan, R. 2021, ApJ, 907, L44

Snios, B., Schwartz, D. A., Siemiginowska, A., et al. 2021, ApJ, 914, 130

Spingola, C., Dallacasa, D., Belladitta, S., et al. 2020, A&A, 643, L12

Tavecchio, F. 2021, MNRAS, 501, 6199

Tavecchio, F., Maraschi, L., Sambruna, R. M., & Urry, C. M. 2000, ApJ, 544, L23

Torres-Albà, N., Bosch-Ramon, V., & Iwasawa, K. 2020, A&A, 635, A57

Weisskopf, M. C., Tananbaum, H. D., Van Speybroeck, L. P., & O'Dell, S. L. 2000, in Society of Photo-Optical Instrumentation Engineers (SPIE) Conference Series, Vol. 4012, X-Ray Optics, Instruments, and Missions III, ed. J. E. Truemper & B. Aschenbach, 2–16

Worrall, D. M. 2009, A&A Rev., 17, 1

Worrall, D. M. & Birkinshaw, M. 2005, MNRAS, 360, 926

Worrall, D. M., Birkinshaw, M., Marshall, H. L., et al. 2020, MNRAS, 497, 988